

# Climate Downscaling: A Deep-Learning Based Super-resolution Model of Precipitation Data with Attention Block and Skip Connections

Chia-Hao Chiang<sup>a</sup>, Zheng-Han Huang<sup>a</sup>, Liwen Liu<sup>a</sup>, Hsin-Chien Liang<sup>b</sup>, Yi-Chi Wang<sup>b</sup>, Wan-Ling Tseng<sup>c</sup>, Chao Wang<sup>a</sup>, Che-Ta Chen<sup>d</sup> and Ko-Chih Wang<sup>a,\*</sup>

<sup>a</sup>Computer Science and Information Engineering, National Taiwan Normal University, Taipei, 116, Taiwan

<sup>b</sup>Research Center for Environmental Changes, Academia Sinica, Taipei, 116, Taiwan

<sup>c</sup>Degree Program in Climate Change and Sustainable Development, National Taiwan University, Taipei, 116, Taiwan

<sup>d</sup>Department of Earth Science, National Taiwan University, Taipei, 116, Taiwan

## ARTICLE INFO

### Keywords:

Climate Downscaling  
Super-resolution  
Machine Learning  
Deep Learning

## ABSTRACT

Human activities accelerate consumption of fossil fuels and produce greenhouse gases, resulting in urgent issues today: global warming and the climate change. These indirectly cause severe natural disasters, plenty of lives suffering and huge losses of agricultural properties. To mitigate impacts on our lands, scientists are developing renewable, reusable, and clean energies and climatologists are trying to predict the extremes. Meanwhile, governments are publicizing resource-saving policies for a more eco-friendly society and arousing environment awareness. One of the most influencing factors is the precipitation, bringing condensed water vapor onto lands. Water resources are the most significant but basic needs in society, not only supporting our livings, but also economics. In Taiwan, although the average annual precipitation is up to 2,500 millimeter (mm), the water allocation for each person is lower than the global average due to drastically geographical elevation changes and uneven distribution through the year. Thus, it is crucial to track and predict the rainfall to make the most use of it and to prevent the floods. However, climate models have limited resolution and require intensive computational power for local-scale use. Therefore, we proposed a deep convolutional neural network with skip connections, attention blocks, and auxiliary data concatenation, in order to downscale the low-resolution precipitation data into high-resolution one. Eventually, we compare with other climate downscaling methods and show better performance in metrics of Mean Absolute Error (MAE), Root Mean Square Error (RMSE), Pearson Correlation, structural similarity index (SSIM), and forecast indicators.

## 1. Introduction

In the past century, human activities have accelerated the consumption of fossil fuels and the emissions of greenhouse gases have drastically increased. Accordingly, the global warming has become an inevitable issue and it relates to the climate changes: desertification, severe droughts, wildfires, flooding to name but a few, showing the climate system has become unstable and irregular. To study climate changes, such as the precipitation trends in the future, one of the common approaches is to develop simulation models. Scientists develop several models to predict climate events to mitigate the impacts of these extremes (website: MIT). Among these models, Global Climate Models (GCMs) are most widely used by climatologists. GCMs are used to simulate future climate patterns by considering the interactions among energy systems of lands, oceans, and atmosphere levels via sophisticated physical and mathematical processes. Although GCMs can provide a long-term, comprehensive climate trend, the computational cost is relatively high. Therefore, scientists often simulate the long-term climate trend with a low-resolution setting to reduce the costs and then feed the GCM results into the climate downscaling methods (e.g., Fowler et al. (2007); Hewitson and Crane

(1996); Xu et al. (2019); Wilby et al. (1998)) to obtain finer results for local-scale uses. Another way to provide more accurate results is to adopt Regional Climate Models (RCMs), as proposed by Rummukainen (2010). These models are capable of generating even higher spatial resolution up to tens of kilometers between data points. Aside from the computational cost, RCMs are not likely to provide general climate patterns since they are sensitive to the given boundary conditions and regional scale forcings (such as land-sea contrast, orography). Some studies show that RCMs perform better in continental regions such as the Great Plains and China, where the forcings are weaker, but perform worse in those with stronger forcings such as New Zealand (e.g., Wang et al. (2004a)). As a result, for even higher resolution needs (several kilometers), a more accurate, skillful method is required for the climate downscaling.

Think beyond the climatology scope, recent studies have addressed the super-resolution (SR) techniques to solve the climate downscaling problems (e.g., Vandal et al. (2017); Kumar et al. (2021); Sharma and Mitra (2022); Passarella et al. (2022); Cheng et al. (2020a); Liu et al. (2020)). Conceptually, SR is equivalent to climate downscaling. SR has been a classic but sophisticated problem in the computer vision field for years. It aims to generate high-resolution images from given low-resolution images. In the following paragraphs, we will use “image upscaling” or “climate

\*The authors are with the Department of Computer Science and Information Engineering, National Taiwan Normal University, Taipei, Taiwan.

\*Corresponding author

✉ kcwang@ntnu.edu.tw (K. Wang<sup>a,\*</sup>)

downscaling” to avoid ambiguity in the process of enlarging the resolution of data.

SR models are mainly built with Convolutional Neural Networks (CNNs) which have been widely used in classification, object detection, natural language processing, etc. Convolutional layers often act as feature extractors and non-linear mappings (with activation functions) to capture information in different levels. Combined with interpolation layers, it is able to reconstruct detailed information from low- to high-resolution images, and it outperforms conventional interpolation methods (e.g., Dong et al. (2015, 2016); Kim et al. (2016); Shi et al. (2016); Kim et al. (2015); Lim et al. (2017); Lai et al. (2017); Ledig et al. (2017)).

With the rapid advancement in machine learning, SR techniques have been continuously evolving and successfully applied to various domains. For instance, they have been utilized for enhancing Computed Tomography (CT) images in medicine (e.g., Ren et al. (2017)), improving the resolution of electron microscopy images in material science (e.g., Sreehari et al. (2016)), and addressing the challenges of enhancing precipitation data in the field of climatology, which is our focus. In recent studies, neural networks have been shown that they are able to skillfully generate satisfying climate downscaling results (e.g., Vandal et al. (2017); Passarella et al. (2022); Cheng et al. (2020a,b); Kumar et al. (2023)). Like the training manner in the image field, in the above approaches, the input is the downsampled or degraded data from its corresponding ground truth. Here we use “homogeneity” to describe such training pairs for example in Fig. 1a. On the contrary, the term “heterogeneity” is used to describe the paired data from difference resources as shown in Fig. 1b. In our study, we are more interested in applying super-resolution to heterogeneous data pairs and the data we use will be introduced in Sec. 4. The heterogeneity problem in super-resolution is more realistic, as there is always a presence of bias between the simulation results and the observations. Therefore, it is crucial to account for and to correct the bias when performing super-resolution.

Although an encoder-decoder network with residual learning is proposed to tackle this climate downscaling problem in a continental region (e.g. Liu et al. (2020)), a new architecture is required for areas with strong climatic forcings. Consequently, we are here to present a newly designed architecture for producing high-quality super-resolution results of precipitation data in such areas. Different from continental regions, island regions or countries often have more complex climate circumstances because they have stronger and more changeable forcings. Besides, these regions could have limited water resources because of insufficient areas for preserving water. Therefore, studying the long-term trends of precipitation in these regions is a challenging and active research topic in climatology (e.g., Nourani et al. (2019); Golian et al. (2022); Ratri et al. (2021)). For example, Taiwan is a subtropical island with only an area of 36,000  $km^2$ , which is only 0.4% of China or the United States. It has strong climatic forcings: the Siberian High and the Pacific Ocean ironical maritime air form the Stationary

Front, southwesterly flows form convective rains in summer, and northeast monsoons bring orographic rains in winter. To more precisely capture the precipitation trend in Taiwan, a huge computational cost is required, which is not cost-efficient. Conventionally, climatologists in Taiwan simulate the long-term precipitation with low resolution and apply climate downscaling methods iteratively to obtain high-resolution results. However, it is still not likely to generate high-quality and realistic outputs from the low-resolution simulations due to unique geographic characteristics and uneven rainfall distribution in Taiwan.

To address the challenges of climate downscaling and bias correction for the small-scale region, we proposed a deep neural network (DNN) consisting of three main parts: convolutional layers, attention blocks, one-step up-scaling layer, and additional auxiliary data (topography data) concatenation shown in Fig.5. Convolutional layers are responsible for bias correction and mapping the input low-resolution data to latent vectors. Attention blocks help to optimize the learning process (e.g., Woo et al. (2018)). The one-step climate downscaling layers combine the learned feature maps and in our approach, we use a pixel shuffle (or pixel rearrangement) layer for image upscaling (e.g., Shi et al. (2016)). Moreover, Daly et al. (1994) have established that topography has a significant impact on precipitation. Therefore, our model takes the high-resolution topographical data as the auxiliary data to facilitate the high-quality climate downscaling results.

Our main contributions are concluded below:

- We propose a deep learning model for heterogeneous precipitation simulation data in climate downscaling problems with bias correction.
- The model is specially designed for an area with strong regional scale forcings and can receive a very small number of precipitation data points from the simulation and generates a corresponding high-resolution output.
- We conducted a comprehensive study and compared it with different types of climate downscaling approaches, including statistical methods and other machine/deep learning approaches to show that ours outperforms alternatives.

## 2. Related Works

In this section, we categorize climate downscaling methods into three classes and discuss below: statistical, dynamic, and machine learning based climate downscaling methods. Also, we briefly introduce the super-resolution models in the image field.

### 2.1. Statistical Climate Downscaling

Von Storch et al. (1993) conducted statistical climate downscaling (SD), relying on statistical correlations between General Circulation Models (GCMs) and regional

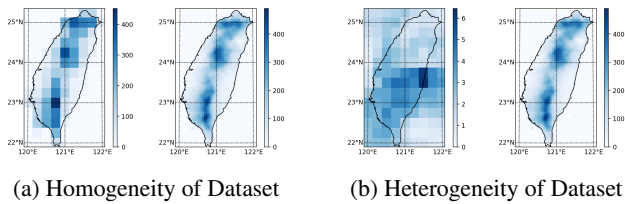


**Figure 1:** Homogeneity and heterogeneity of the datasets. (a) Homogeneous data pair. One can still tell that the low-resolution one (downsampled one, on the left-hand side) is similar to the high-resolution one (original data, on the right-hand side). The downsampled data is structural similar to the origin one, that there are same patterns at corresponding regions, but only with some lacks of high-frequency information in low-resolution one. (b) Heterogeneous data pair. It is hard to tell the structural similarity between them through patterns, since one is from ERA5 reanalysis data (left-hand side), and the other is from observations (right-hand side). Neither patterns nor the value ranges are similar.

historical observational data. It assumes that the relationship is constant and defines predictand as a function of the predictor. This type of approach can be divided into two steps: empirically establish the statistical relationship between the simulation results and local variables (e.g., Wilby and Wigley (2000); Chu et al. (2008)), and then apply this relationship to the simulation results to map to local-scale climate variables, including precipitation, air pressure, or temperature.

There are many ways to perform SD tasks. For example, regression models such as the generalized linear model (e.g., McCullagh (2019)) have been widely used to fit probability distributions (e.g., Fealy and Sweeney (2007); Bergin et al. (2012, 2015)). The non-homogeneous Hidden Markov Model (NHMM), introduced by Zucchini and Guttorp (1991), tries to relate rainy occurrences (e.g., Mehrotra and Sharma (2005); Greene et al. (2011); Khalil et al. (2010); Nyongesa et al. (2020)). Two SD methods, Quantile Mapping (QM) and Bias Corrected Spatial Disaggregation (BCSD) researched by Thrasher et al. (2012), are widely used in coupling GCMs and historic observations. QM tries to derive corrected precipitation values by matching the cumulative distribution functions (CDFs) of the biased one and non-biased one (e.g., Cannon et al. (2015)). BCSD further optimizes QM by adding a Spatial Disaggregation step, where the corrected values are interpolated based on the average of the corresponding days, rather than themselves. However, SD methods can only get the spatially finer data. Since the original data are GCM outputs, they do not consider the detailed influences of the landform, soil, or vegetation. In other words, regional climate mechanisms are omitted during the process. Therefore, as the scaling factor increases, the biases become larger and cause spatial shifts on the grid points.

## 2.2. Dynamic Climate Downscaling

Dynamic climate downscaling, or the Regional Climate Models (RCMs), are similar to GCMs. Both are formulated

on physical principles, but RCMs focus on a smaller, local scale climate simulations rather than the global ones. “Dynamic” represents the interactions between physical and chemical variables of RCMs. Due to such environmental interactions, the main downside of this approach is the huge computational costs. To generate regional predictions, scientists will feed RCMs with GCMs simulation results as the boundary conditions. Significantly, different boundary condition settings generate distinguishing climate patterns, so do the area size and resolution, and each setting gives limited climate patterns in local. Moreover, with limited resources, there is a trade-off between spatial or temporal resolution.

Although RCMs have powerful comprehension upon local features, there are still systematic errors, leading to large uncertainties (e.g., Themeßl et al. (2012)). To correct such errors, some ensemble methods are proposed for improving RCMs, but they require collaboration of institutions due to the intensive computation and integration (e.g., Fu et al. (2005); van der Linden P. and (eds.); Mearns et al. (2009)).

## 2.3. Single-Image Super-Resolution with CNNs

Single-image super-resolution (SISR) is a classic application in the image processing field by Yang et al. (2019). The popularity of deep learning has skyrocketed in recent decades, leading to the successive proposal of various architectures for SISR. Among these models, convolutional neural networks (CNNs) are the most popular one.

Dong et al. (2015) proposed the very first end-to-end CNN-based SISR model, known as Super Resolution Convolutional Neural Network (SRCNN). Subsequently, Dong et al. (2016) also proposed an improved version of SRCNN, named Fast Super-Resolution Convolutional Neural Networks (FSRCNN), which can perform SISR without the bicubic upscaling process in SRCNN. Shi et al. (2016) used the pixel rearrangement (pixel shuffle) method as the image upscaling layer to build Efficient Sub-pixel Convolutional Neural Networks (ESPCN). It uses a one-step image upsampling layer which reduces the number of model parameters while maintaining reliable performance. Kim et al. (2016) proposed Very Deep Super Resolution networks (VDSR) that features residual learning (skip connections) (e.g., He et al. (2015)). Another work called Deeply-Recursive Convolutional Network (DRCN) introduced by Kim et al. (2015), is the first to apply the Recursive Neural Network (RNN) architecture to SR problems. Mao et al. (2016) proposed Residual Encoder-Decoder Network (RED-Net) which contains an architecture of convolutional (encoders) and deconvolutional (decoders) layers with symmetrically multiple skip connections, which is the first approach in image restoration by using these two layers.

In addition, Lai et al. (2017) applied a cascade of convolutional layers for feature extraction and deconvolutional layers for image upscaling. It features in progressive reconstruction of SR predictions, using Laplacian pyramids. Ledig et al. (2017) set a new state-of-the-art on public benchmark datasets by introducing the Generative Adversarial Network

(GAN) architecture for SISR. It borrows the VGG layers from Simonyan and Zisserman (2014) to replace commonly used loss function such as MSE, and defines a so-called VGG loss which is like a perceptual similarity function between feature representations and generated images.

#### 2.4. Deep Learning Based Climate Downscaling

In recent years, more and more climate models have adopted super-resolution techniques in SISR field to climate datasets for further analysis. The main difference from image and climate data is the theoretically unlimited minimum and maximum values of the channels, or parameter values. Fortunately, with some modifications, it once again shows the capabilities of deep learning.

DeepSD, proposed by Vandal et al. (2017) is one of the very first deep learning models that tries to perform the climate downscaling of precipitation data. It is modified from SRCNN, but in a stacked manner. For example, divide a scale factor of 8 into three  $\times 2$  blocks. It also takes the topography data as an input channel, taking the geographical influences into account. Some variants of DeepSD are proposed for easier training and faster outputs (e.g., Kumar et al. (2021); Sharma and Mitra (2022)). Beyond precipitation data, Passarella et al. (2022) tried training a modified FSRCNN model, named FSRCNN-ESM, which takes earth system model simulations as input. They added additional convolutional layers after the deconvolution step in the FSRCNN to improve the climate downscaling performance.

Cheng et al. (2020a) introduced a residual dense block to LapSRN network. One can collect different scales of high-resolution results at corresponding level. They also conducted a detailed study of checkerboard artifacts elimination in parameter studies of deconvolutional layers.

Similar to the progress in SISR field, one of the latest climate downscaling methods is SRGAN-based model which turns out to outperform other types of models like DeepSD, Augmented Convolutional Long Short Term Memory (ConvLSTM), LapSRN, and U-Net (e.g., Cheng et al. (2020b); Kumar et al. (2023)).

However, all models above are trained with homogeneous pairs, that is, degraded one as input, and identical one as ground truth. As mentioned in Sec. 1, we use the term, homogeneity, as that there are a few differences between the input (low resolution) and output (high resolution), meaning that we can still tell the patterns or structures by traditional interpolations like bilinear or bicubic. On the contrary, we are trying to construct a model to capture the relationships between the reanalysis precipitation data and the corresponding observation data which are obviously not from the same data source, saying a heterogeneous pair. Addressing the heterogeneous dataset, YNet, as developed by Liu et al. (2020), used GCMs simulations and reanalysis data for the training. Yet, YNet tackled this climate downscaling problem in a continental region, which has a weak climatic forcings. Therefore, we have to consider a new architecture to cover both heterogeneity and strong climatic forcings which will be elaborated in Sec. 3.

### 3. Methods

The main purpose of this work is to get a high-resolution result  $\mathbf{Y}$ , given a low-resolution input  $\mathbf{X}$ , which can be simplified as:  $\mathbf{Y} = Model(\mathbf{X}; \Theta)$ , where  $\Theta$  is the hyper-parameters of the model. Our model comprises a series of convolutional layers with residual attention blocks as our model spine, skip connections of feature maps at different levels, and a one-step image upscaling layer, as shown in Fig. 5. These parts are introduced in the following subsections.

#### 3.1. Cascading Convolutional Bias Correction

We utilize a cascade of convolutional layers to fulfill the tasks of bias correction and feature extractions as shown in Fig. 5a. Given a low-resolution input  $\mathbf{X} \in \mathbb{R}^{H \times W \times C}$ , a convolutional layer outputs a feature map  $\mathbf{F} \in \mathbb{R}^{H \times W \times f}$ , where  $H$ ,  $W$ , and  $C$  are height, width, and the number of input channels and  $f$  is the number of filters, respectively. It can be formulated as Eq.(1):

$$\begin{aligned} \mathbf{F}_0 &= act(W * \mathbf{X} + bias), \text{ and} \\ \mathbf{F}_i &= act(W_i * \mathbf{F}_{i-1} + bias_i) \quad \forall i \in \mathbb{N}^+ \end{aligned} \quad (1)$$

for subsequent layers, where  $\mathbf{F}_i$  is the intermediate feature map of  $i^{th}$  layer,  $(*)$  denotes the convolution operation, and  $act(\cdot)$  as the activation function. We can see there is a bias term in the operation, exactly what we expect to be analogous to statistical climate downscaling methods (QM), where the CDF and its inverse are replaced by a nonlinear mapping, as shown in Eq.(2).

$$x_{i,j}^{cor} = W_n * (\mathbf{F}_{n-1}(\dots(\mathbf{F}_0(x_{i,j}^{bias})\dots))) + bias_n \quad (2)$$

#### 3.2. Skip Connections

To avoid gradient diminishing for training a DNN, skip connections have been widely used for both residual learning and decreasing training parameters.

As shown in Fig. 5b, let  $\mathbf{F}(x)$  be the desired mapping of input  $x$ , and the residual learning is reforming the nonlinear mapped into  $\mathbf{F}(x) - x$  (Fig. 2). It is said to be easier in optimizing the residuals than original mapping. To a extreme that the mapping is identical, to learn a zero residual is easier than to fit the original one by stacked non-linear layers (e.g., He et al. (2015)). Inspired from Zhang et al. (2018), to make the most use of the feature maps extracted from previous layers, and to avoid gradient diminishing, we also apply several skip connections in our model in Fig. 5b. We extract the feature maps from convolutional layers and apply a shrinkage layer for lessening the number of parameters. These extracted maps are then connected to a fusion layer before climate downscaling.

#### 3.3. Residual Attention Block

We adopt the Channel Block Attention Module (CBAM) proposed by Woo et al. (2018) in Fig. 5c. CBAM has two sub-modules: Channel Attention Block (CAB) and Spatial Attention Block (SAB). These two blocks help our model to

learn “what to emphasize” and “where to focus” respectively, and emphasize the extracted features by multiplying to input feature map.

CAB consists of a pair of max-pooling and average pooling, and a shared multi-layer perceptron (MLP) unit, as shown in Fig. 4b. SAB consists of a pair of channel-wise max-pooling and average pooling and a convolutional layer, as shown in Fig. 4c. Given an intermediate feature map of the  $i$ -th layer  $\mathbf{F}_i \in \mathbb{R}^{H \times W \times f}$ , CAB gives a 1D attention map  $M_c \in \mathbb{R}^{1 \times 1 \times f}$ , while a 2D one  $M_s \in \mathbb{R}^{H \times W \times 1}$  is generated by SAB. The refined feature maps  $\mathbf{F}_{i,c}$  and  $\mathbf{F}_{i,s}$ , are summarized as Eq.(3):

$$\begin{aligned} \mathbf{F}_{i,c} &= M_c \otimes \mathbf{F}_i \\ \mathbf{F}_{i,s} &= M_s \otimes \mathbf{F}_i, \end{aligned} \quad (3)$$

where  $\otimes$  denotes the element-wise multiplication. For  $M_c$ , it is broadcasted along spatial dimension. We found that it has better performance when arranging in a sequential manner, and we added a connection from  $\mathbf{F}_i$  to construct the so-called Residual Attention Block (RAB) shown in Fig. 4a. The final refined feature map  $\mathbf{F}'_i$  is shown in Eq.(4):

$$\mathbf{F}'_i = \mathbf{F}_i \oplus (M_s \otimes \mathbf{F}_{i,c}), \quad (4)$$

where  $\oplus$  denotes the element-wise addition.

### 3.4. One-step Image Upscaling Layer

We use the pixel shuffle method from ESPCN (Fig. 3) and attach another convolutional layer to mitigate the blocky results as shown in Fig. 5d. Pixel shuffle, or pixel rearrangement, is to push the subpixels along the channel axis to the spatial field. For example, an intermediate output with  $r^2$  number of filters is fed into pixel shuffle layer which gives a  $rH \times rW$  upscaled results. It has more modeling capabilities than other image upscaling methods. Others such as bilinear, bicubic and deconvolutional layer may generate blurred images or severe checkerboard artifacts. Bilinear and bicubic interpolation produce blurry results and do not consider spatial relationship between grid points, which may result in distorted outputs. While in deconvolutional layer, the uneven kernel overlapping issue occurs, resulting in checkerboard artifacts especially when its kernel size is not divisible by the stride (e.g., Odena et al. (2016)). We will also compare the performance of different image upscaling layer in Sec. 5.

### 3.5. Implementation Details

We normalized the training data and elevation by log1p transformation:  $x' = \ln(x + 1)$  to handle the long-tail distribution property of precipitation, and no batch-normalization during the training process. In our model, all convolutional layers are set with  $3 \times 3$  kernel size throughout our model backbone, along with 64 filters, strides by 1 and valid paddings (zero paddings), except a  $5 \times 5$  kernel size in SAB, and a  $1 \times 1$  kernel size in shrinkage layers. A rectified linear unit (ReLU), proposed by Nair and Hinton (2010), is used as an activation function after each convolutional layer except

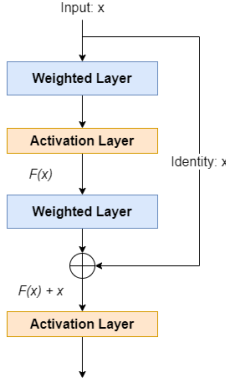


**Figure 2:** A simple building block with a skip connections. The skip connection (or “shortcut connection”) is to feed forward an identity  $x$  to the output of a series of layers. It is commonly used in a deep neural network for training optimization.

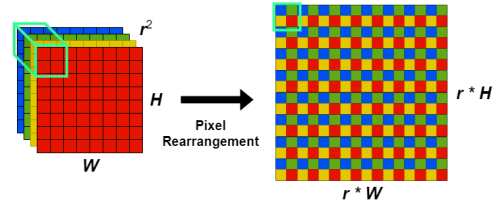


**Figure 3:** Pixel shuffle from ESPCN. This one-step upscaling layer rearranges the pixels along channel axis into a larger image. The number of channels needs to be adjusted to the square of the scaling factor. One can change the number of filters of the convolutional layer right before pixel shuffle layer for preferred scaling factor.

the last one and the one in the attention blocks, where a sigmoid activation is applied.

We extract intermediate feature maps from every two convolutional layers into the attention block, which consists of a pair of sequentially arranged CAB and SAB. The shared MLP of CAB is set to be 256 nodes, a reduction factor of 0.5, and the output nodes are equal to the number of channels, in a total of three dense layers. The RAB outputs are then fed into shrinkage layers. Subsequently, we concatenate them and feed them into a fusion layer, obtaining an output channel of 1 for the element-wise addition with skip connections from the local input, namely the residual learning mechanism.

Next, we feed into a pixel shuffle layer for climate downscaling. Notice that we add a convolutional layer immediately after it to alleviate checkerboard artifacts. Eventually, we append several convolutional layers again for the elevation data fusion to generate the final result of climate-downscaled precipitation data.

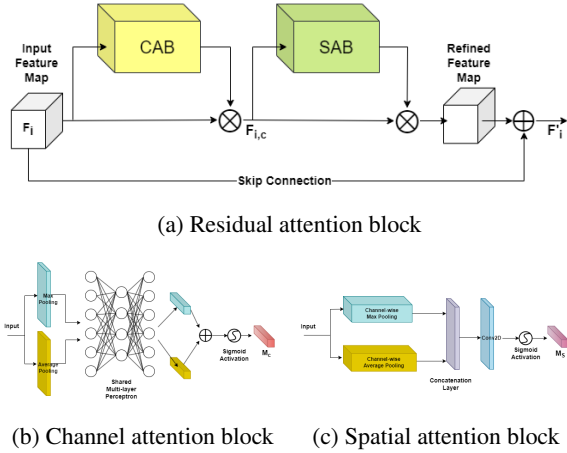


**Figure 4:** Diagram of attention blocks. As illustrated in (a), a residual attention block (RAB) consists of a channel attention block (CAB) and a spatial attention block (SAB), and a skip connection from input feature map forwarding to refined feature map. (b) shows the structure of CAB, including a global max pooling, a global average pooling, and a shared multi-layer perceptron unit. (c) illustrates the structure of SAB, including a pair of channel-wise max and average pooling, a concatenation layer, and a convolutional layer. Both activation functions in (b) and (c) are using sigmoid activation.

## 4. Dataset

Continuing with the heterogeneity and strong climatic forcings, we found Taiwan is a suitable study area to showcase our model capabilities. Taiwan is an island in subtropics, extending about 400 km from north to south and 150 km from east to west with only an area of 36,000 km<sup>2</sup>, about 4% large of China. Mountains run along north-south manner and most of rivers flow east to west. The monsoon season starts from April to October, mainly contributed by plum rains in May to June and typhoon rains in July to September. While in northern cities, northeast monsoon also causes orographic rain in winter. Despite the average annual rainfall being up to 2,500 mm, which is 2.5 times than the global average, the water resource is insufficient, even lower than the global average. Such insufficiency is attributed to geographical characteristics and uneven rainfall distribution throughout the year.

We are taking ERA5 reanalysis data as our training input, pairing with TCCIP observations as ground truth, and train our model in a supervising manner. The reason is that since the upscaling factor is minimal for simulations to downscale into observations in Taiwan area, we are not using GCMs or RCMs as our model input, or the upscaling factor would be up to nearly a hundred.

The following subsections introduce the attributes and dimensions of the data:

### 4.1. ERA5 Reanalysis Data

ERA5 dataset is produced using Four-Dimensional Variational Data Assimilation (4D-Var) and model forecasts of the European Center for Medium-Range Weather Forecasts

(ECMWF) Integrated Forecast System (IFS). It is a kind of reanalysis data, which combines a large number historical observations into global simulation estimates. Climatologists often adopt ERA5 dataset for research to understand climate change and current weather extremes (website: ERA5). The spatial unit of ERA5 dataset is represented in meters, and the time span is from the 1950 to 2020, hourly. For each daily piece, the global precipitation values are stored in a matrix with the size of 1440×720 along longitude and latitude.

### 4.2. TCCIP Precipitation Data

We take gridded precipitation data from TCCIP (published on May 1, 2020.) as our high-resolution data, which is from the Taiwan Climate Change Projection Information and Adaptation Knowledge Platform (TCCIP). The dataset is rasterized based on the observatory data, collected from Taiwan Central Weather Bureau, Water Resources Agency, and Civil Aeronautics Administration. There are two different spatial resolutions available: 0.05° and 0.01°. The 0.05° one means that the distance between neighboring data points is around 5 km, covering from latitude 21.9°N to 25.2°N and longitude 120.0°E to 122.0°E, with the size of 69×41. While 0.01° one means that the distance between neighboring data points is around 5 km, covering from latitude 21.9°N to 25.2°N and longitude 120.0°E to 122.0°E, with the size of 69×41. Data are recorded daily, from 1960 to 2020, 22,281 days in total, and the precipitation unit is in millimeters. More information is available at the TCCIP website.

### 4.3. Topographical Data

Terrains are one of the most important factors in climatology, which affects air convection, lift, and flow. For example, orographic precipitation is formed when moist air is forced to rise along the windward side of mountains and then becomes cooled, condensed, and eventually forms clouds. On the contrary, the leeward side would encounter dry winds, even Foehn winds. Therefore, our model also takes elevation information from the terrain to predict the high-resolution data. We use the terrain data from the Center for Geographic Information System, the Research Center for Humanities and Social Sciences, Academia Sinica as shown in Fig. 6. The resolution of the data is 0.01° (1 km), with the resolution of 480×371, latitude from 21.5042°N to 25.4958°N, and longitude from 119.2042°E to 122.2875°E. The altitude range is from -36.930 to 3706.753 meters.

### 4.4. Data Preprocessing

To align with our TCCIP precipitation data (high-resolution data), ERA5 reanalysis data (low-resolution data) is converted to daily average and multiply with 10<sup>3</sup> to get daily average precipitation data (unit: mm) with spatial resolution of 0.25° (around 25 km), and choose from the year 1960 to 2020, in a total of 22,281 time steps. Furthermore, since we are only interested in the data points in Taiwan, we crop the data covering Taiwan island only, with a size of 14×9 per day, as low-resolution inputs.

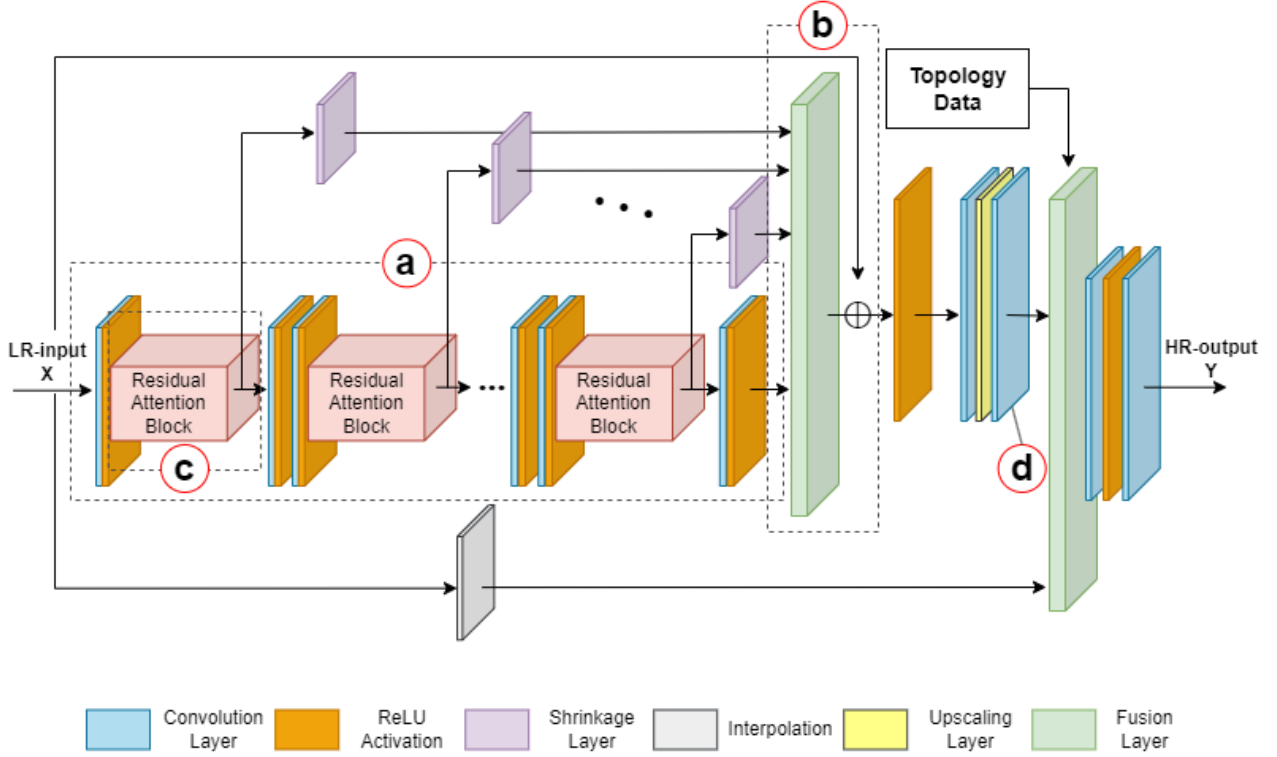


**Figure 5:** Overview of proposed model architecture. Main stream of the model is a series of residual attention block, attached with a convolutional layer and a ReLU activation. Refined intermediate feature maps are fed into a convolutional layer with  $1 \times 1$  kernel size to limit the number of parameters and pick up the most significant one at different levels for forwarding. The first fusion layer combines all refined feature maps, while the second one additionally concatenate elevation data and interpolation of original input. The image upscaling layer is adopting the pixel shuffle technique from ESPCN, after a convolutional layer with the number of filters equal to square of scaling factor.

For TCCIP data, we zero out the on-sea values and align the data points with the cropped ERA5 dataset near Taiwan island. The TCCIP data is cropped from latitude  $22.0^\circ\text{N}$  to  $25.25^\circ\text{N}$  and longitude  $120.0^\circ\text{E}$  to  $122.0^\circ\text{E}$  by nearest neighboring interpolation. Filtered data ends up with a resolution of  $66 \times 41$  and each data point represents the precipitation data in a  $5 \times 5 \text{ km}^2$  region.

Regarding the terrain data, we also take the latitude and longitude with  $22.0042^\circ\text{N}$  to  $25.2542^\circ\text{N}$ ,  $120.0042^\circ\text{E}$  to  $122.0042^\circ\text{E}$ , with the size of  $391 \times 241$ , and mask out the negative values elevation data points (lower than sea level).

## 5. Experiment

### 5.1. Setup

#### 5.1.1. Model Implementation

We implemented our model in the Tensorflow framework. There are a total of 22,281 daily precipitation data and are randomly separated by 80% for training, 10% for validation, and the other 10% for testing. The batch size is set to be 64 and an epoch is limited to a maximum training loop by 1,000 with an early-stop setting by patience equal to 60. We use the mean square error (MSE) as our loss function Eq. (5). The model training is optimized by Adam Optimizer

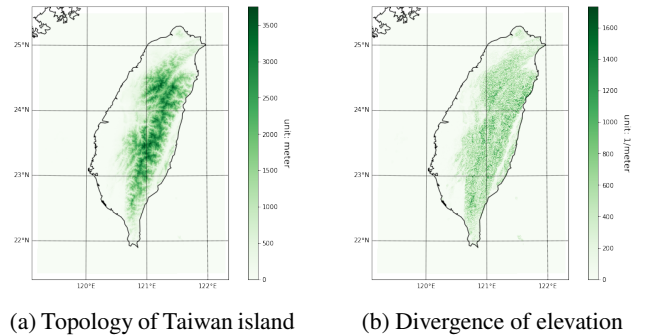


**Figure 6:** Topology of Taiwan island. (a) Study area in Taiwan. Taiwan is an island in subtropics. It extends about 400 km from north to south and 150 km from east to west. Altitudes are shown in meters. It shows the mountains run along north-south manner and therefore most of rivers flow from east to west. (b) Drastic elevation changes in Taiwan. The figure shows the divergence value of each data point,  $\nabla_{x,y}$ . By considering the neighboring altitudes along longitude and latitude, divergence is calculated as the square root of slopes in units of  $\text{meters}^{-1}$ .

with default settings and a learning rate of  $10^{-4}$ . The training

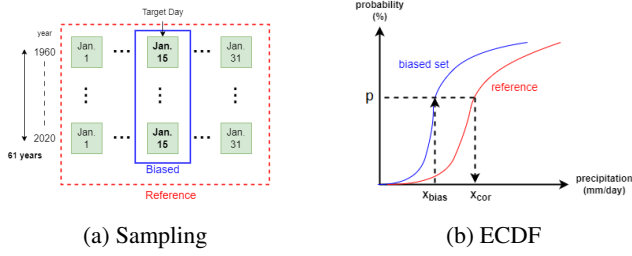


**Figure 7:** Bias correction with Empirical Quantile Mapping. (a) Sampling of biased and reference data. To construct the ECDFs in (b), the CDF of biased one is obtained based on the target date through 61 years (1960 - 2020) (blue rectangle), and the CDF of reference one is based on whole days within the window through all years (red rectangle). (b) ECDFs of biased and reference data. The blue curve is the CDF of biased data, while the red one is the CDF of reference data. A corrected value  $x_{cor}$  is derived from the relationship between the CDF of biased data (bilinearly interpolated) and the CDF of reference one. This process is performed through every grid point of the biased data. Given a biased grid point  $x_{bias}$  in target day, the cumulative probability  $p$  is obtained according to the CDF of biased data. With the value of  $p$ , the corrected value  $x_{cor}$  is obtained from the inverse function of the CDF of reference data.

process was performed on NVIDIA® Tesla V100 GPU.

$$MSE = \frac{1}{H \times W} \sum_{i=1}^H \sum_{j=1}^W \|\hat{Y}_{i,j} - Y_{i,j}\|^2 \quad (5)$$

where  $H$  and  $W$  are the height and width of the prediction, and  $\hat{Y}_{i,j}$  is the corresponding ground truth of the prediction  $Y_{i,j}$ .

### 5.1.2. Metrics

Peak Signal to Noise Ratio (PSNR) is a commonly used metric in the image field. But in scientific data, since there is no theoretical maximum value, PSNR may not meet our needs. Hence, we use mean absolute error (MAE), root mean square error (RMSE), Pearson Correlation (Corr.), and structural similarity index (SSIM) proposed by Wang et al. (2004b) as our metrics. Lower MAE and RMSE indicate better accuracy between the predictions and observations, while higher Pearson Correlation and SSIM indicate stronger relationships between the predictions and observations.

Also, we evaluate the results with forecast indicators: Probability of Detection (POD), False Alarm Ratio (FAR) and Threat Score (TS) (e.g., DOSWELL et al. (1990); Murphy (1996)). The threshold is set as 0.1 mm for calculating the forecast indicators, as a critical value of rainfall existence, to calculate indicators. A higher POD indicates a higher percentage of correctly predicted events, and a higher TS indicates a higher skill in capturing both hits and correct negatives, while minimizing false alarms and misses. A lower FAR indicates a lower percentage of false alarms or incorrect forecasts.

### 5.1.3. Alternative Approaches

We pick two statistical climate downscaling methods: QM by Cannon et al. (2015) and BCSD by Thrasher et al. (2012). Additionally, we re-train other three deep learning based models, DeepSD, FSRCNN-ESM, and YNet for comparison. We briefly introduce the QM and BCSD algorithm below: let  $x_{i,j}^{bias}$  be the biased value of precipitation at a grid point  $(i, j)$  in the  $k^{th}$  day. And let  $F_{i,j}^{bias}$  be the CDF of the grid point in biased dataset, and  $F_{i,j}^{ref}$  of reference, correspondingly. To get the corrected value  $x_{i,j}^{cor}$  take the value in reference dataset of the same CDF value as corrected one, that is:

$$x_{i,j}^{cor} = InvF_{i,j}^{ref} [F_{i,j}^{bias}(x_{i,j}^{bias})] \quad \forall x_{i,j}^{bias} \in X_k^{bias} \quad (6)$$

where  $InvF(\cdot)$  is the inverse of CDF,  $X_k^{bias}$  is the set of biased grid points in the  $k^{th}$  day, as shown in Fig. 7b. In general, the correction is based on the resolution of the biased dataset, and in this case the reference dataset is degraded to 25 km, the same as the biased one. Also, the CDF of the target day is calculated on each grid point over the years within a time window. The window size is set to be 15 as TCCIP (published on May 1, 2020.) suggested, that is, before and after the  $k^{th}$  day,  $k \pm 15$ . We then take all the data within the window over years as to-be-corrected one, and corresponding days over reference one to get  $F^{ref}$ , as shown in Fig. 7a.

BCSD algorithm further adds a Spatial Disaggregation (SD) step after QM shown in Eq. (7). SD step performs the interpolation of the difference of target daily rainfall  $X_k^{cor}$  and the average of degraded reference  $Y_l$ . Then, multiply with the SD factor, which is the ratio between the means of original reference rainfall  $Y_h$  and the degraded one  $Y_l$ . Eventually, add original reference to the product mentioned above to get the final value  $Z_k$ , which is:

$$Z_k = Y_h + Intp(X_k^{cor} - Y_l) * \frac{Y_h}{Y_l + 1} \quad (7)$$

where  $Intp(\cdot)$  is the interpolation method, and  $\frac{Y_h}{Y_l + 1}$  is the scaling factor which is modified by plus one to avoid unrealistic value of dry days.

## 5.2. Results

The predictions of various climate downscaling methods with different scaling factors are shown in Table 1. Our model performs better in the metrics and indicators, except the POD in each scaling factor. We notice that BCSD has the highest POD values, which is **1.0000**. It is because POD only considers the number of points that predictions and corresponding ground truths are both greater than the threshold (0.1 mm). To an extreme case, if the prediction is all ones, the POD would also be **1.0000**. This overestimation might result from the multiplication in Eq. (7). And we can tell such errors from the other two indicators, FAR and TS. As for DeepSD and FSRCNNESM, after we re-train them with our dataset, they results in lower performance. Since YNet was



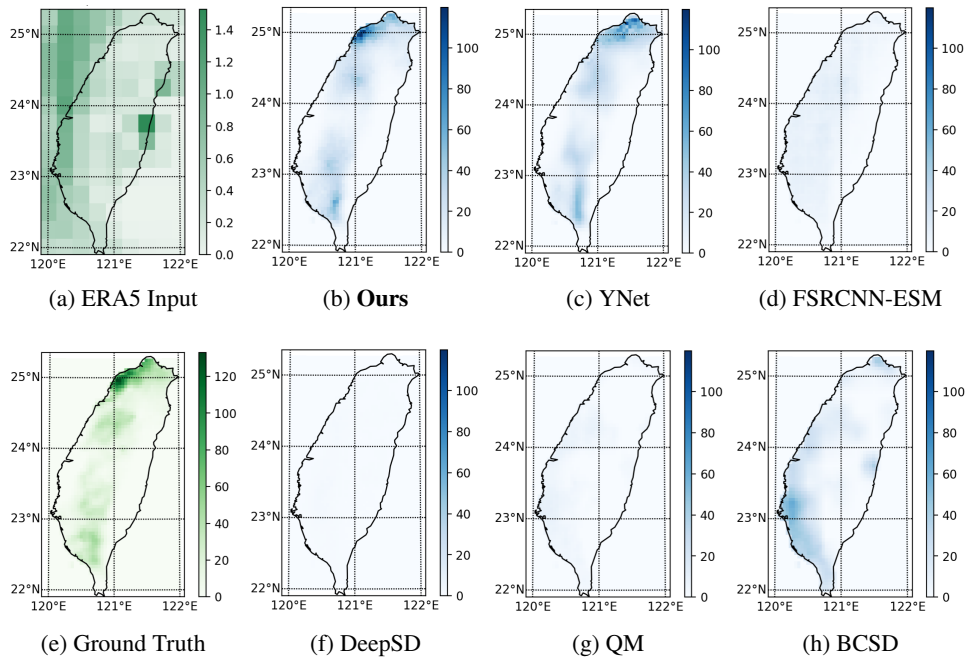


**Figure 8:** Predictions of an extremely concentrated precipitation case with different climate downscaling methods (scaling factor = 5). (a) The input data of ERA5 reanalysis from ECMWF. (e) The observations from TCCIP, as our ground truth data. Notice that the range of colormap of (a) and (e) are different in order to more clearly show the significant bias problem between the input and corresponding observation. Other subfigures show the super-resolutions with different climate downscaling methods whose color map ranges are aligned with the ground truth's. The deeper blue is, the larger value is. Both (b) and (c) are able to capture the real precipitation range and main spatial distribution in north Taiwan. However, for (d) (f) and (g), the predictions values are pretty low, showing the main challenges in bias correction. As for (h), since it adds the Spatial Disaggregation step with corresponding mean value of observations Eq. (7), the value range are closer to the ground truth, but still fails to predict the main precipitation patterns.

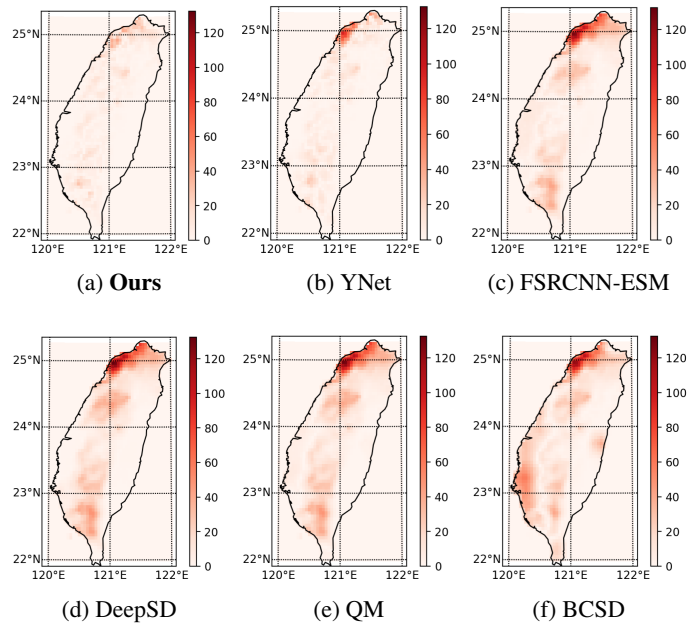


**Figure 9:** MAEs of an extremely concentrated precipitation case with different climate downscaling methods (scaling factor = 5). Continued with Fig. 8, the subfigures show the differences (MAEs) between ground truth and SR results of different climate downscaling methods. The deeper red is, the larger difference is, and the more similar to the image pattern of ground truth is, the worse performance it is. The ground truth precipitation values are distributed in the west of Taiwan, and specifically, higher values in north-west part. Ours shows the lowest MAE among all predictions.

initially designed and evaluated in continental precipitation ensemble data, for single channel and non-continental data, ours shows better performance in such scenario.

Among the results, we pick three representatives of precipitation distribution in Taiwan, ordered by the concentration of precipitation. Cooperated with the domain experts, the model with the scaling factor of 5 is looked for in current climatological research, since the resolution of the first-hand observation data is the closest to this factor. Therefore, we pick this scaling factor for showcases.

Fig. 8 shows the predictions of extremely concentrated rainy day in Jun. 14, 2016. The ERA5 reanalysis data in Fig. 8a infers a concentrated rain at Hualian city (23.8°N, 121.4°E), while the corresponding ground truth in Fig. 8e concentrates at Taoyuan city (25°N, 121°E). For other cities, there are scattered rainfall in the west, but it merely rains in the east. Our model is able to do the correction of concentrated rainy spots and adjust to realistic precipitation values (Fig. 8b). Although YNet also corrects the concentrated rainy locations, the precipitation values are lower predicted (Fig. 8c). While others like FSRCNN-ESM and DeepSD predicts much lower precipitation values that they shows nearly zeros covering the whole island, and so do QM and BCSD methods. Fig. 9 clearly shows the differences between realistic precipitation values and predictions. The second example in Fig. 10 shows the predictions of a heavy rain over the entire Taichung city (the central part of Taiwan) in May 19, 2019. Similarly, our model has predicted correctly for the main rainy regions, and has corrected to realistic precipitation values. Although YNet also corrects the concentrated rainy locations, the precipitation area are smaller predicted (Fig. 10c). While others are unable to correct to realist values, except BCSD which has multiplied with the scaling factor between observations and biased data in Eq. (7) but the rainfall location is not correctly predicted. The last example in Fig. 12 shows the predictions of a relatively even-distributed light rains over north and east part of Taiwan in Apr. 18, 2016. The rainy regions are pretty scattered and discrete precipitation makes the errors of predictions be shown in a spotty pattern (Fig. 13). Ours and YNet are giving an east rainfall distribution correctly but are failed to precisely capture the discrete patterns. Since the loss function is set as MSE, it tends to generate a smoother result. In other words, it might be difficult for models to precisely predict a discrete, scattered pattern.

### 5.3. Parameter Study

To find optimal model structure, we did the following parameter studies below, including model size, type of upscaling layer and showed significant influences of the topography:

#### 5.3.1. Model Size: Number of Layers

As a general insight of machine learning, model size or the number of hyperparameters is highly correlated to output quality. Smaller model might end up with higher losses and poor capability, while larger model has more flexibility, but may cause overfitting. We can tell if the model size is proper

for the scenario through comparisons of the training and validation losses of different model sizes. We tested three different numbers of convolutional layers in our model spine, that is 16, 32, and 48, to find the most suitable size for our configuration. The training and validation losses are shown in Fig. 15. The 48-layer one stops the earliest, but has higher losses than the 32-layer one, which may inform the difficulties in optimization. The highest losses occur in the 16-layer one which indicates its lack of capability among others in handling the climate downscaling of heterogeneous data.

After training, we feed testing data for evaluations, and eventually pick the 32-layer one as our base, since it has the lowest MAE and RMSE and highest Corr. and SSIM, as shown in Fig. 14. The configuration might vary with different data properties, but we offer a reference setting to the climate downscaling task.

#### 5.3.2. Image Upscaling Layers

As mentioned in Sec. 3, different image upscaling layers would influence the quality of climate downscaling results. Concerns are that bilinear and bicubic methods usually do not provide any “new” information to data, while deconvolutional layers and the pixel shuffling layer will encounter the checkerboard artifacts if the kernel size is not divisible by the number of strides (e.g., Odena et al. (2016); Cheng et al. (2020a)). Although both bilinear and bicubic are non-learnable parameters in the model, they will influence other learnable ones. For example, we were expecting our model to learn a low-resolution, but an intermediate output whose bias has been corrected right before the bilinear or bicubic layer. Yet, the climate downscaling of heterogeneous data might be more complicated. Hence, we verified four upscaling layers: bilinear, bicubic, deconvolutional layer, and pixel rearrangement to find the best-fitting one. The results are shown in Fig. 16. The medians of bicubic one has the highest MAE and RMSE and the lowest Pearson Correlation and SSIM. Besides, it has larger deviations, which shows the unstable predictions. While, the pixel shuffling (pixel rearrangement) has the lowest MAE and RMSE, the highest Pearson Correlation and SSIM, and smaller deviation, showing relatively stable predictions. Therefore, we adopt pixel shuffling layer as our image upscaling method.

#### 5.3.3. Topography Data

As mentioned in Sec. 1, we show the enhancement of climate downscaling results by adding a concatenation layer with terrain data in Fig. 17. It shows statistically significant difference in whether to concatenate with the topography data. This implies that there are strong influences or correlations with precipitation, and that the neccessariness of topography data in the climate downscaling task. Our model successfully capture such interaction between precipitation and topography, resulting in better prediction quality.

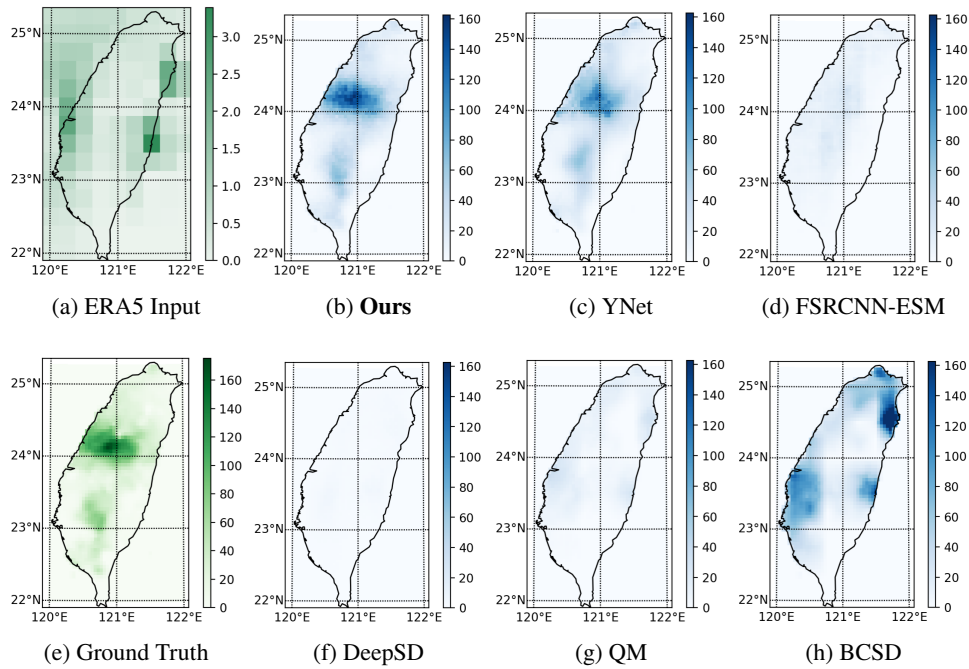


**Figure 10:** Predictions of an uneven distributed precipitation case with different climate downscaling methods (scaling factor = 5). (a) The input data of ERA5 reanalysis from ECMWF. (e) The observations from TCCIP, as our ground truth data.

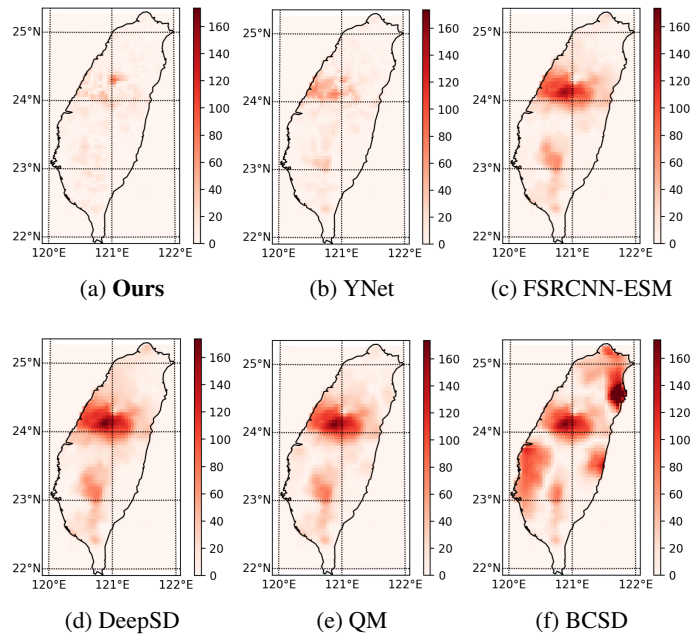


**Figure 11:** MAEs of an uneven distributed precipitation case with different climate downscaling methods (scaling factor = 5). Continued with Fig. 10, the subfigures show the differences (MAEs) between ground truth and SR results of different climate downscaling methods. The deeper red is, the larger difference is, and the more similar to the image pattern of ground truth is, the worse performance it is.

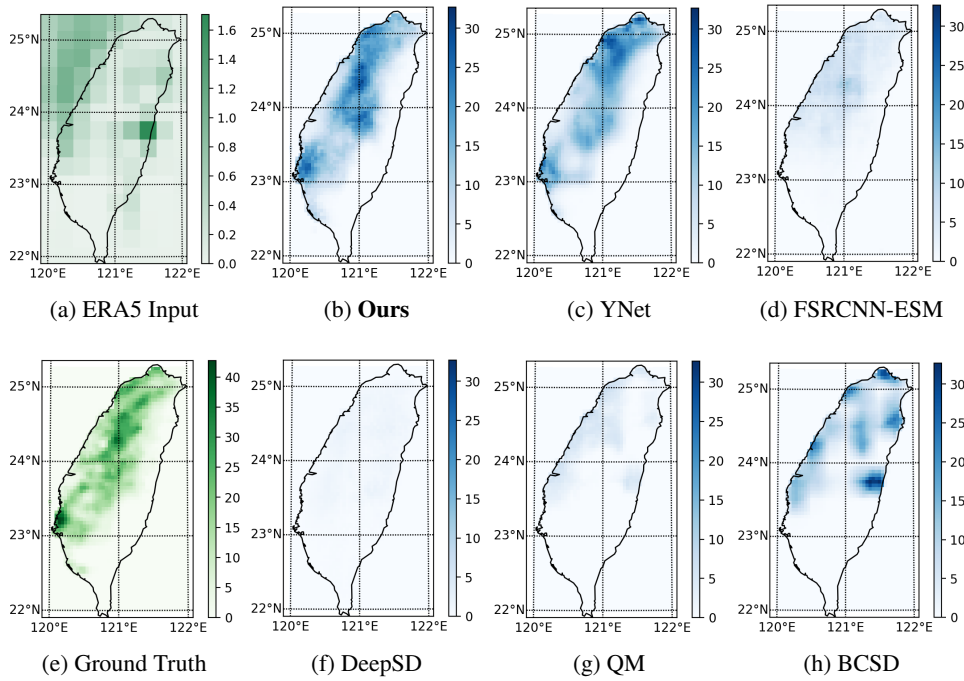


**Figure 12:** Predictions of a relatively even distributed precipitation case with different climate downscaling methods (scaling factor = 5). (a) The input data of ERA5 reanalysis from ECMWF. (e) The observations from TCCIP, as our ground truth data.

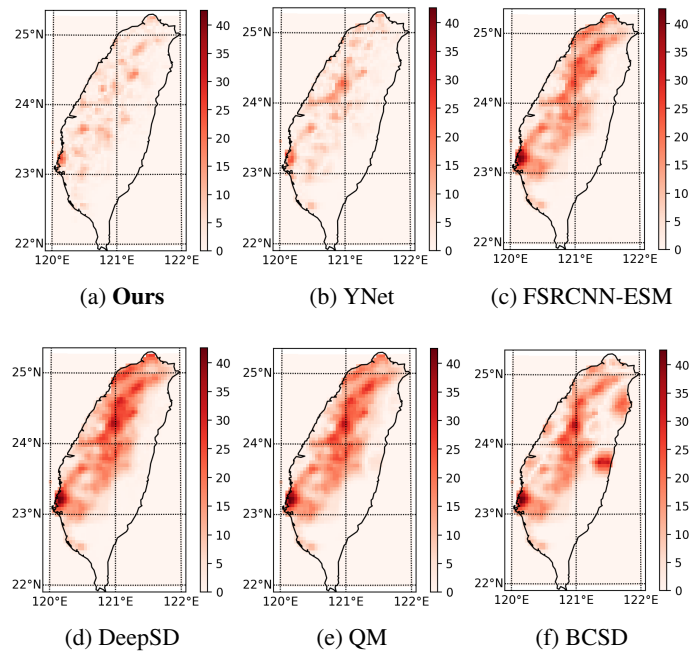


**Figure 13:** MAEs of a relatively even distributed precipitation case (scaling factor = 5). Continued with Fig. 12, the subfigures show the differences (MAEs) between ground truth and SR results of different climate downscaling methods. The deeper red is, the larger the difference is, and the more similar to the image pattern of ground truth is, the worse performance it is.

A Deep-Learning Model for Heterogeneous Precipitation Data Downscaling

Scaling Factor	Downscaling Method	Metrics (Avg. / Med.)				Indicators (Avg. / Med.)		
		MAE	RMSE	Corr.	SSIM	POD	FAR	TS
x2	QM	5.2078	9.0507	0.3532	0.4108	0.5919	0.4915	0.4129
		1.3397	3.8916	0.3364	0.3610	0.5000	0.4265	0.2937
	BCSD	5.2564	8.3366	0.3618	0.1043	<b>1.0000</b>	0.7170	0.3102
		1.9838	3.6999	0.3235	0.0609	<b>1.0000</b>	0.8306	0.1694
	DeepSD	4.8107	8.3481	0.3352	0.1310	0.9876	0.7037	0.3254
		1.1039	2.9429	0.3278	0.1179	<b>1.0000</b>	0.8049	0.1947
FSRCNN-ESM	4.0904	7.1279	0.4601	0.2319	0.9952	0.7056	0.3233	
	1.1011	2.7516	0.4616	0.2087	<b>1.0000</b>	0.8091	0.1907	
YNet	1.9920	4.1826	0.6978	0.6427	0.8491	0.4580	0.5708	
	0.6409	2.0600	0.8179	0.6510	0.9143	0.4000	0.5345	
Ours	<b>1.6884</b>	<b>3.5713</b>	<b>0.7526</b>	<b>0.6921</b>	0.8428	<b>0.4093</b>	<b>0.6052</b>	
	<b>0.5429</b>	<b>1.7454</b>	<b>0.8703</b>	<b>0.7272</b>	0.9091	<b>0.3412</b>	<b>0.5801</b>	
x4	QM	5.4020	8.8380	0.3474	0.5739	0.5630	0.4801	0.3922
		1.3402	3.8548	0.3237	0.5516	0.4737	0.4375	0.2727
	BCSD	5.2238	8.2537	0.3539	0.2084	<b>1.0000</b>	0.7128	0.2983
		1.9871	3.6458	0.3198	0.1812	<b>1.0000</b>	0.8318	0.1682
	DeepSD	5.0753	8.9770	0.2822	0.2598	0.9724	0.7051	0.3089
		1.1408	2.9387	0.2664	0.2604	<b>1.0000</b>	0.8170	0.1821
FSRCNN-ESM	3.9873	7.0270	0.4279	0.3455	0.9891	0.7010	0.3109	
	1.1154	2.7751	0.4306	0.3296	<b>1.0000</b>	0.8068	0.1924	
YNet	1.9588	4.1685	0.6369	0.5634	0.7992	0.5278	0.4937	
	0.6780	2.1344	0.7938	0.5647	0.9105	0.4930	0.4745	
Ours	<b>1.6979</b>	<b>3.6271</b>	<b>0.6917</b>	<b>0.6625</b>	0.8382	<b>0.4598</b>	<b>0.5600</b>	
	<b>0.5813</b>	<b>1.8998</b>	<b>0.8369</b>	<b>0.6624</b>	0.9210	<b>0.4098</b>	<b>0.5439</b>	
x5	QM	4.5550	7.9047	0.3766	0.6121	0.5138	0.4401	0.3636
		1.2571	3.5200	0.3660	0.5955	0.5655	0.3828	0.3474
	BCSD	4.4342	7.4289	0.4256	0.4067	0.6277	0.5356	0.3672
		1.8717	3.7533	0.4017	0.4059	0.7500	0.5301	0.3379
	DeepSD	5.0695	8.7594	0.2062	0.6116	0.6805	0.5952	0.3607
		0.8996	2.9104	0.1629	0.6445	0.7680	0.6262	0.3154
FSRCNN-ESM	4.9565	8.6558	0.1801	0.6764	0.4899	0.3922	0.3672	
	0.8655	2.9678	0.1211	0.7272	0.5377	0.3130	0.3487	
YNet	1.6101	3.4145	0.7112	0.7955	<b>0.7208</b>	0.3932	0.5405	
	0.4616	1.4945	0.8573	0.8416	<b>0.8728</b>	0.3153	0.6083	
Ours	<b>1.1469</b>	<b>2.9352</b>	<b>0.7391</b>	<b>0.8300</b>	0.7149	<b>0.3372</b>	<b>0.5635</b>	
	<b>0.4172</b>	<b>1.3532</b>	<b>0.8832</b>	<b>0.8644</b>	0.8658	<b>0.2629</b>	<b>0.6384</b>	
x8	QM	5.0429	8.7130	0.3292	0.6855	0.4540	0.4855	0.3153
		1.3394	3.7770	0.2909	0.6969	0.4556	0.4557	0.2636
	BCSD	5.2495	8.2898	0.3407	0.2084	<b>1.0000</b>	0.7106	0.2894
		1.9730	3.6179	0.2934	0.1812	<b>1.0000</b>	0.8306	0.1694
	DeepSD	5.3036	9.3460	0.2598	0.4005	0.9632	0.6997	0.2994
		1.1991	3.0452	0.2338	0.3931	0.9981	0.8111	0.1883
FSRCNN-ESM	4.5037	7.7278.	0.3329	0.3609	0.9876	0.7050	0.2948	
	1.2432	2.9157	0.3268	0.3577	0.9997	0.8218	0.1782	
YNet	1.9893	4.2271	0.6167	0.8230	0.6406	0.4227	0.4985	
	0.5815	1.9557	0.7707	0.8501	0.8231	0.3193	0.5776	
Ours	<b>1.7077</b>	<b>3.6412</b>	<b>0.6827</b>	<b>0.8647</b>	0.6667	<b>0.2955</b>	<b>0.5522</b>	
	<b>0.4964</b>	<b>1.7104</b>	<b>0.8273</b>	<b>0.8849</b>	0.8309	<b>0.2183</b>	<b>0.6470</b>	

**Table 1**

Metrics and climate indicators of different climate downscaling methods with different scaling factors. Metrics include MAE, RMSE, Pearson Correlation, and SSIM. Climate indicators include POD, FAR, and TS. The threshold of precipitation detection is set as 0.1 mm. One has the best performance if it has lower MAE, RMSE and FAR as well as higher Corr., SSIM, POD and TS.

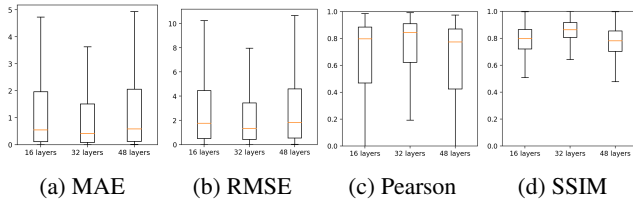


**Figure 14:** Model performance of different number of layers. It shows that the 32-layer one has lower MAE and RMSE, higher Pearson Correlation and SSIM. It also implies the proper model size (number of parameters) in aspect of model capability and avoiding overfitting problems.

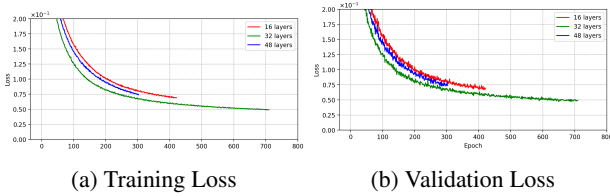


**Figure 15:** Losses of different number of layers. The training hyperparameters are set as epochs = 1,000, batch size = 64, and with an early stopping = 60. The 48-layer one has higher losses than the 32-layer one, which reflects the difficulties in optimization. While the 16-layer one has the highest losses, this indicates the lack of capability.

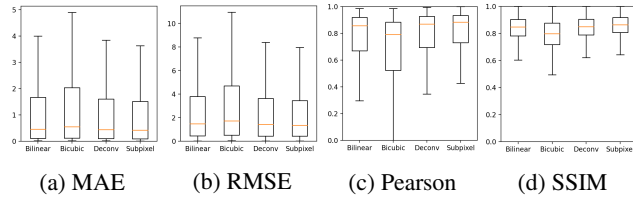


**Figure 16:** Boxplots of different upscaling layers. As mentioned in Sec. 3, we show the performance of different types of image upscaling layer here. It turns out to be that the pixel shuffling (subpixel) image upscaling method has the best prediction quality.

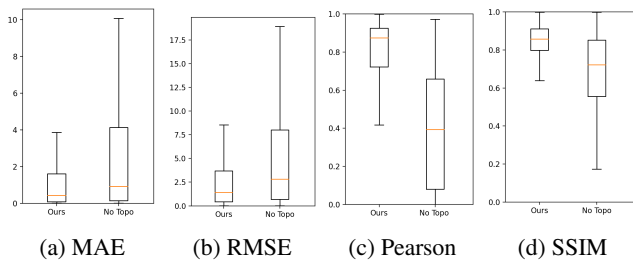


**Figure 17:** Boxplots of whether to concatenate with topography. It shows statistically significant difference in whether to adopt the topography data. This implies there are strong influences in precipitation as mentioned in Sec. 1, and our model successfully capture such interaction between precipitation and topography.

## 6. Conclusion

In this paper, we proposed a deep learning based climate downscaling model for the precipitation data in a strong climatic forcing, non-continental, and topographically drastic changing area. We have tackled with the data heterogeneity and severe bias problems between reanalysis data and observations. For our model training, we collected and picked ERA5 reanalysis data and TCCIP gridded observational data. Our model is mainly composed of a series of convolutional layers and utilizes several residual attention blocks, skip connections and concatenation of topography data to better catch the relations of regional climatic forcings to precipitation. Furthermore, we compared the predictions with two commonly-used statistical climate downscaling methods and other three machine learning based ones in metrics of MAE, RMSE, Corr. and SSIM, as well as the forecast indicators, POD, FAR and TS. And we have shown that our model has better performance among all the other methods.

Evidently, machine learning does bring skillful solutions to climate downscaling issues, but lack of physical, climatological explanations of how the climate patterns are determined. After all, the model is seen as a black box, and that is another interesting topic in interpretable or explainable AI field. For instance, by analyzing the intermediate layer outputs, we may use techniques like saliency maps to capture global or local explanations and help climatologists to fine-tune the simulation models. Combined with some visualization and interpretable techniques, it may help the climate science community to study uncertainties and climate patterns. For example, it would be more easily to manipulate climate analysis by developing a customized visualization tool which may also provide the public more comprehensive, straightforward, and understandable insights into our sophisticated climate systems. Another research direction could be an integrated model for the climate downscalings of simulation data like GCMs rather than reanalysis data to observations. After all, the cross-domain applications of machine learning are thriving nowadays. The potentiality is still awaiting the discovery and excavation.

## References

- Bergin, E., Buytaert, W., Kwok-Pan, C., Turner, A., Chawla, I., Mujumdar, P., 2015. Using satellite products to evaluate statistical downscaling with generalised linear models, in: EGU General Assembly Conference Abstracts, p. 5667.
- Bergin, E., Buytaert, W., Onof, C., Wheeler, H., 2012. Downscaling of rainfall in peru using generalised linear models, in: World congress on water, climate and energy. Dublin, Ireland.
- Cannon, A.J., Sobie, S.R., Murdock, T.Q., 2015. Bias correction of gcm precipitation by quantile mapping: how well do methods preserve changes in quantiles and extremes? *Journal of Climate* 28, 6938–6959.
- Cheng, J., Kuang, Q., Shen, C., Liu, J., Tan, X., Liu, W., 2020a. Reslap: Generating high-resolution climate prediction through image super-resolution. *IEEE Access* 8, 39623–39634.
- Cheng, J., Liu, J., Xu, Z., Shen, C., Kuang, Q., 2020b. Generating high-resolution climate prediction through generative adversarial network. *Procedia Computer Science* 174, 123–127.
- Chu, J.L., Kang, H., Tam, C.Y., Park, C.K., Chen, C.T., 2008. Seasonal forecast for local precipitation over northern taiwan using statistical downscaling. *Journal of Geophysical Research: Atmospheres* 113.
- CKB, . “copernicus knowledge base: Era5 data documentation”. <https://confluence.ecmwf.int/display/CKB/ERA5>. (accessed Mar. 14, 2023), (“CKB” stands for the CAMS and C3S Knowledge Base.).
- Daly, C., Neilson, R.P., Phillips, D.L., 1994. A statistical-topographic model for mapping climatological precipitation over mountainous terrain. *Journal of Applied Meteorology and Climatology* 33, 140–158.
- Dong, C., Loy, C.C., He, K., Tang, X., 2015. Image super-resolution using deep convolutional networks. *IEEE transactions on pattern analysis and machine intelligence* 38, 295–307.
- Dong, C., Loy, C.C., Tang, X., 2016. Accelerating the super-resolution convolutional neural network. *CoRR abs/1608.00367*. URL: <http://arxiv.org/abs/1608.00367>, arXiv:1608.00367.
- DOSWELL, C., Davies-Jones, R., Keller, D.L., 1990. On summary measures of skill in rare event forecasting based on contingency tables. *Weather and forecasting* 5, 576–585.
- Fealy, R., Sweeney, J., 2007. Statistical downscaling of precipitation for a selection of sites in ireland employing a generalised linear modelling approach. *International Journal of Climatology: A Journal of the Royal Meteorological Society* 27, 2083–2094.
- Fowler, H.J., Blenkinsop, S., Tebaldi, C., 2007. Linking climate change modelling to impacts studies: recent advances in downscaling techniques for hydrological modelling. *International Journal of Climatology: A Journal of the Royal Meteorological Society* 27, 1547–1578.
- Fu, C., Wang, S., Xiong, Z., Gutowski, W.J., Lee, D.K., McGregor, J.L., Sato, Y., Kato, H., Kim, J.W., Suh, M.S., 2005. Regional climate model intercomparison project for asia. *Bulletin of the American Meteorological Society* 86, 257–266.
- GFDL, . “global climate models, geophysical fluid dynamic laboratory”. <https://www.gfdl.noaa.gov/climate-models/>. (accessed June 26, 2023), (“GFDL” stands for Geophysical Fluid Dynamics Laboratory, which is hosted by Princeton University Forrestal Campus.).
- Golian, S., Murphy, C., Wilby, R.L., Matthews, T., Donegan, S., Quinn, D.F., Harrigan, S., 2022. Dynamical–statistical seasonal forecasts of winter and summer precipitation for the island of ireland. *International Journal of Climatology* 42, 5714–5731.
- Greene, A.M., Robertson, A.W., Smyth, P., Triglia, S., 2011. Downscaling projections of indian monsoon rainfall using a non-homogeneous hidden markov model. *Quarterly Journal of the Royal Meteorological Society* 137, 347–359.
- He, K., Zhang, X., Ren, S., Sun, J., 2015. Deep residual learning for image recognition. *CoRR abs/1512.03385*. URL: <http://arxiv.org/abs/1512.03385>, arXiv:1512.03385.
- Hewitson, B.C., Crane, R.G., 1996. Climate downscaling: techniques and application. *Climate Research* 7, 85–95.
- Khalil, A.F., Kwon, H.H., Lall, U., Kaheil, Y.H., 2010. Predictive downscaling based on non-homogeneous hidden markov models. *Hydrological Sciences Journal–Journal des Sciences Hydrologiques* 55, 333–350.
- Kim, J., Lee, J.K., Lee, K.M., 2015. Deeply-recursive convolutional network for image super-resolution. *CoRR abs/1511.04491*. URL: <http://arxiv.org/abs/1511.04491>, arXiv:1511.04491.
- Kim, J., Lee, J.K., Lee, K.M., 2016. Accurate image super-resolution using very deep convolutional networks, in: *Proceedings of the IEEE conference on computer vision and pattern recognition*, pp. 1646–1654.
- Kumar, B., Atey, K., Singh, B.B., Chattopadhyay, R., Acharya, N., Singh, M., Nanjundiah, R.S., Rao, S.A., 2023. On the modern deep learning approaches for precipitation downscaling. *Earth Science Informatics* , 1–14.
- Kumar, B., Chattopadhyay, R., Singh, M., Chaudhari, N., Kodari, K., Barve, A., 2021. Deep learning–based downscaling of summer monsoon rainfall data over indian region. *Theoretical and Applied Climatology* 143, 1145–1156.
- Lai, W.S., Huang, J.B., Ahuja, N., Yang, M.H., 2017. Deep laplacian pyramid networks for fast and accurate super-resolution, in: *2017 IEEE Conference on Computer Vision and Pattern Recognition (CVPR)*, pp. 5835–5843. doi:10.1109/CVPR.2017.618.
- Ledig, C., Theis, L., Huszár, F., Caballero, J., Cunningham, A., Acosta, A., Aitken, A., Tejani, A., Totz, J., Wang, Z., et al., 2017. Photo-realistic single image super-resolution using a generative adversarial network, in: *Proceedings of the IEEE conference on computer vision and pattern recognition*, pp. 4681–4690.
- Lim, B., Son, S., Kim, H., Nah, S., Mu Lee, K., 2017. Enhanced deep residual networks for single image super-resolution, in: *Proceedings of the IEEE conference on computer vision and pattern recognition workshops*, pp. 136–144.
- van der Linden P., (eds.), J.M., 2009. *Ensembles: Climate change and its impacts: Summary of research and results from the ensembles project.* .
- Liu, Y., Ganguly, A.R., Dy, J., 2020. Climate downscaling using ynet: A deep convolutional network with skip connections and fusion, in: *Proceedings of the 26th ACM SIGKDD International Conference on Knowledge Discovery & Data Mining*, pp. 3145–3153.
- Mao, X.J., Shen, C., Yang, Y.B., 2016. Image restoration using convolutional auto-encoders with symmetric skip connections. *arXiv preprint arXiv:1606.08921* .
- McCullagh, P., 2019. *Generalized linear models*. Routledge.
- Mearns, L.O., Gutowski, W., Jones, R., Leung, R., McGinnis, S., Nunes, A., Qian, Y., 2009. A regional climate change assessment program for north america. *Eos, Transactions American Geophysical Union* 90, 311–311.
- Mehrotra, R., Sharma, A., 2005. A nonparametric nonhomogeneous hidden markov model for downscaling of multisite daily rainfall occurrences. *Journal of Geophysical Research: Atmospheres* 110.
- MIT, . “climate modeling, programs in atmospheres, oceans and climate (poac)”. <http://paocweb.mit.edu/research/climate/climate-modeling>. (accessed June 26, 2023), (“MIT” stands for Massachusetts Institute of Technology.).
- Murphy, A.H., 1996. The finley affair: A signal event in the history of forecast verification. *Weather and forecasting* 11, 3–20.
- Nair, V., Hinton, G.E., 2010. Rectified linear units improve restricted boltzmann machines, in: *Proceedings of the 27th international conference on machine learning (ICML-10)*, pp. 807–814.
- Nourani, V., Uzelaltinbulat, S., Sadikoglu, F., Behfar, N., 2019. Artificial intelligence based ensemble modeling for multi-station prediction of precipitation. *Atmosphere* 10, 80.
- Nyongesa, A.M., Zeng, G., Ongoma, V., 2020. Non-homogeneous hidden markov model for downscaling of short rains occurrence in kenya. *Theoretical and Applied Climatology* 139, 1333–1347.
- Odena, A., Dumoulin, V., Olah, C., 2016. Deconvolution and checkerboard artifacts. *Distill URL: http://distill.pub/2016/deconv-checkerboard*, doi:10.23915/distill.00003.
- Passarella, L.S., Mahajan, S., Pal, A., Norman, M.R., 2022. Reconstructing high resolution esm data through a novel fast super resolution convolutional neural network (fsrcnn). *Geophysical Research Letters* 49, e2021GL097571.
- Ratri, D.N., Whan, K., Schmeits, M., 2021. Calibration of ecmwf seasonal ensemble precipitation reforecasts in java (indonesia) using bias-corrected precipitation and climate indices. *Weather and Forecasting* 36,

- 1375–1386.
- Ren, H., El-Khamy, M., Lee, J., 2017. CT-SRCNN: cascade trained and trimmed deep convolutional neural networks for image super resolution. CoRR abs/1711.04048. URL: <http://arxiv.org/abs/1711.04048>, arXiv:1711.04048.
- Rummukainen, M., 2010. State-of-the-art with regional climate models. *Wiley Interdisciplinary Reviews: Climate Change* 1, 82–96.
- Sharma, S.C.M., Mitra, A., 2022. Resdeepd: A residual super-resolution network for deep downscaling of daily precipitation over india. *Environmental Data Science* 1, e19.
- Shi, W., Caballero, J., Huszár, F., Totz, J., Aitken, A.P., Bishop, R., Rueckert, D., Wang, Z., 2016. Real-time single image and video super-resolution using an efficient sub-pixel convolutional neural network, in: *Proceedings of the IEEE conference on computer vision and pattern recognition*, pp. 1874–1883.
- Simonyan, K., Zisserman, A., 2014. Very deep convolutional networks for large-scale image recognition. arXiv preprint arXiv:1409.1556 .
- Sreehari, S., Venkatakrisnan, S.V., Bouman, K.L., Simmons, J.P., Drummy, L.F., Bouman, C.A., 2016. Multi-resolution data fusion for super-resolution electron microscopy. CoRR abs/1612.00874. URL: <http://arxiv.org/abs/1612.00874>, arXiv:1612.00874.
- TCCIP, . “taiwan climate change projection information and adaptation knowledge platform (tccip), coordinated by national science and technology center for disaster reduction (ncdr)”. [https://tccip.ncdr.nat.gov.tw/ds\\_03\\_eng.aspx](https://tccip.ncdr.nat.gov.tw/ds_03_eng.aspx). (accessed July 30, 2022), (“TCCIP” stands for The Taiwan Climate Change Projection Information and Adaptation Knowledge Platform.).
- TCCIP, published on May 1, 2020. “rasterization of daily observational precipitation data in taiwan”. [https://tccip.ncdr.nat.gov.tw/km\\_newsletter\\_one.aspx](https://tccip.ncdr.nat.gov.tw/km_newsletter_one.aspx). (accessed Mar. 1, 2023), (“TCCIP” stands for The Taiwan Climate Change Projection Information and Adaptation Knowledge Platform.).
- Thiemeßl, M.J., Gobiet, A., Heinrich, G., 2012. Empirical-statistical downscaling and error correction of regional climate models and its impact on the climate change signal. *Climatic Change* 112, 449–468.
- Thrasher, B., Maurer, E.P., McKellar, C., Duffy, P.B., 2012. Bias correcting climate model simulated daily temperature extremes with quantile mapping. *Hydrology and Earth System Sciences* 16, 3309–3314.
- Vandal, T., Kodra, E., Ganguly, S., Michaelis, A., Nemani, R., Ganguly, A.R., 2017. DeepSD: Generating high resolution climate change projections through single image super-resolution, in: *Proceedings of the 23rd acm sigkdd international conference on knowledge discovery and data mining*, pp. 1663–1672.
- Von Storch, H., Zorita, E., Cubasch, U., 1993. Downscaling of global climate change estimates to regional scales: an application to iberian rainfall in wintertime. *Journal of Climate* 6, 1161–1171.
- Wang, Y., Leung, L.R., McGREGOR, J.L., Lee, D.K., Wang, W.C., Ding, Y., Kimura, F., 2004a. Regional climate modeling: progress, challenges, and prospects. *Journal of the Meteorological Society of Japan. Ser. II* 82, 1599–1628.
- Wang, Z., Bovik, A.C., Sheikh, H.R., Simoncelli, E.P., 2004b. Image quality assessment: from error visibility to structural similarity. *IEEE transactions on image processing* 13, 600–612.
- Wilby, R.L., Wigley, T., 2000. Precipitation predictors for downscaling: observed and general circulation model relationships. *International Journal of Climatology: A Journal of the Royal Meteorological Society* 20, 641–661.
- Wilby, R.L., Wigley, T., Conway, D., Jones, P., Hewitson, B., Main, J., Wilks, D., 1998. Statistical downscaling of general circulation model output: A comparison of methods. *Water resources research* 34, 2995–3008.
- Woo, S., Park, J., Lee, J.Y., Kweon, I.S., 2018. Cbam: Convolutional block attention module, in: *Proceedings of the European conference on computer vision (ECCV)*, pp. 3–19.
- Xu, Z., Han, Y., Yang, Z., 2019. Dynamical downscaling of regional climate: A review of methods and limitations. *Science China Earth Sciences* 62, 365–375.
- Yang, W., Zhang, X., Tian, Y., Wang, W., Xue, J.H., Liao, Q., 2019. Deep learning for single image super-resolution: A brief review. *IEEE Transactions on Multimedia* 21, 3106–3121. doi:10.1109/TMM.2019.2919431.
- Zhang, Y., Tian, Y., Kong, Y., Zhong, B., Fu, Y., 2018. Residual dense network for image super-resolution, in: *Proceedings of the IEEE conference on computer vision and pattern recognition*, pp. 2472–2481.
- Zucchini, W., Guttorp, P., 1991. A hidden markov model for space-time precipitation. *Water Resources Research* 27, 1917–1923.